Micro-Doppler Signatures of Dynamic Humans From Around The Corner Radar

Shelly Vishwakarma, Aaquib Rafiq, and Shobha Sundar Ram
Indraprastha Institute of Information Technology Delhi
New Delhi, India 110020
{shellyv,aaquibr,shobha}@iiitd.ac.in

***Abstract*—Recent studies have demonstrated the possibility of sensing dynamic targets around the corners with no direct signal in line-of-sight with respect to the radar. These works have mostly focused on the detection of targets around the corner on the basis of multipath scattering from lateral walls. However, strong specular multipath returns are only obtained for highly conductive walls or at high carrier frequencies. There is minimal research effort into using the existing indoor radar hardware at much lower carrier frequencies for around the corner sensing of targets. In this paper, we have performed a detailed experimental analysis, including both simulations and measurements, of the effect of wall parameters and carrier frequency on the around the corner micro-Doppler signatures of dynamic humans. Our results demonstrate that in real world scenarios where walls are lossy, target micro-Dopplers are weak and distorted by multipath scattering at high carrier frequencies and are sensed only very near the radar. At lower carrier frequencies, the targets are sensed at greater distances and the micro-Dopplers are not significantly distorted by multipath since the signals mostly travel along the direct path through the wall.**

***Index Terms*—Through-wall radar, around the corner radar, FDTD, micro-Doppler signatures**

I. Introduction

In recent years, sensing targets around the corner of walls and other types of blockages by radar is being increasingly researched for surveillance purposes [1]–[4]. The *around the corner* radar (ACR) is relatively new when compared to *through wall* radar (TWR) [5] and indoor radar [6] technologies. Indoor radars are typically characterized by low carrier frequencies and bandwidths of the order of few hundreds of MHz, resulting in range resolution in the order of meters. These radars have usually relied on Doppler information for inferring the type of activity undertaken by the target [7], [8] while in [9], [10], the range and azimuth information have been gathered for localizing and imaging the target. Detection and localization of targets in ACR are considerably complicated by the complex electromagnetic propagation phenomenology of the radar signals, as shown in Fig.1. At low frequencies, the radar signal may propagate through the blockage (such as a wall). There may be diffraction around edges of the blockage as well as multipath signals arising from specular reflections off the surface of the blockages. As a result, the radar signatures - the high range resolution profiles and the Doppler spectrograms - may be considerably distorted.

Measurements of ACR radar data have been previously conducted at S-band [11], X band [12] and Ku bands [13]. In [12], the authors demonstrated that micro-Doppler signatures of humans could be generated in non line-of-sight (NLOS) conditions using stepped frequency continuous waveforms while in [13], the authors proposed a detection and localization strategy based on generalized likelihood ratio test applied on multipath returns. In [11], the authors used WiFi signals to detect moving targets around corners. Along with measurement data collection, there have also been several efforts to model ACR data. Prior works have mostly simulated ACR scattering by modeling walls as perfect electric conductors [14], [15]. This assumption is mostly valid when the radars operate at high carrier frequencies (X, Ku), where wall materials are highly lossy. In these conditions, the radar scatterings consist of strong specular multipath returns and very weak direct path signals through the walls. Therefore, these works have modeled radar returns using ray tracing. However, if ACR data are to be collected from existing hardware systems developed for TWR purposes or other ubiquitous low-frequency wireless networks such as WiFi, then the direct path signal through the wall cannot be ignored. The resulting ACR signatures will consist of features arising from all three of the propagation mechanisms shown in Fig.1. In this paper, we study the propagation effects for realistic wall parameters on signatures generated from both simulated and measured ACR data.

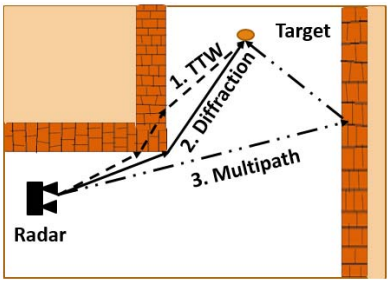

Fig. 1. Propagation mechanisms for around the corner radar include propagation of radar signals through the walls (TTW), diffraction around the corners and multipath scattering off lateral walls.

We simulate the signal propagation phenomenology of an around-the-corner radar using a full-wave electromagnetic solver based on finite difference time domain (FDTD) techniques for four different carrier frequencies in S, C, X and Ku bands. Our previous works have demonstrated methods to simulate both narrowband [16] and broadband radar [17] returns from humans in TWR environments for both a single antenna element and an antenna array [18]. Here, the wall propagation phenomenology, modeled using finite difference time domain techniques (FDTD), and primitive based models of humans, are hybridized to generate the radar returns. We adapt the method to simulate the ACR radar returns of a human. First, we consider a single point scatterer moving with constant velocity and study the Doppler returns for different wall parameters such as the dielectric constant, the conductivity, the thickness, and the width of the walls. Then we simulated micro-Dopplers of a human moving along a trajectory such that the human is always under non-line-of-sight conditions. We provide a comparison to the micro-Doppler signatures obtained in free space scenarios. Finally, we present experimental results of micro-Doppler data gathered from around-the-corner radar scenarios for the three carrier frequencies and provide a comparison of the resulting signatures with those obtained under line-of-sight conditions. Our results show that the Doppler returns are most sensitive to the carrier frequency of the signal and the

978-1-7281-6813-5/20/$31.00 ©2020 IEEE

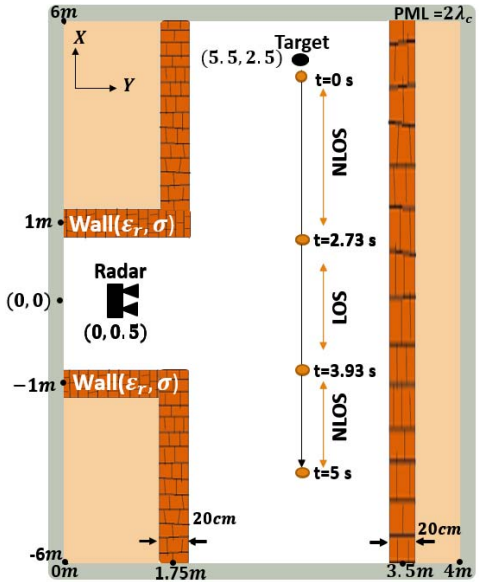

Fig. 2. Trajectory followed by a point scatterer in FDTD space.

conductivity of the wall. At low carrier frequencies, walls are not very lossy, and the Doppler returns are mostly identical to those obtained under free space scenarios. However, at high frequencies the multipath signals arising from specular reflections off the lateral walls give rise to additional Doppler components. The strength of the returns is a function of the reflectivity of the walls. When the walls are not very conductive, the multipath returns are weak and the distance at which the target's micro-Doppler is observed is quite low.

Our paper is organized as follows. In section II, we describe the simulation set up based on FDTD for obtaining the radar returns of a point scatterer and for an extended human target in an around-the-corner radar scenario for different carrier frequencies. We present the simulated radar micro-Doppler signatures for different ACR scenarios. In section III, we present the experimental set up for measurement data collection of a human monitored by an ACR radar and the related results. Section IV concludes the paper.

II. Simulation Experiments

We simulate the electromagnetic propagation phenomenology for the ACR radar using a two-dimensional FDTD based full wave solver. The geometry of the simulation space is shown in Fig.2. The space spans 12m along X and 4m along Y. There are three walls that segment the space into two rooms (highlighted with a different color) and a *T-shaped* white corridor space. The walls are $20cm$ thick, and the corridor spans 1.55m in its width. The source in the FDTD simulation is assumed to be located at the radar position at $(0, 0.5)$m and excited by a narrowband source of λ_c wavelength corresponding to a carrier frequency f_c. The entire two-dimensional space is bounded by a perfectly matched layer (PML) of $2\lambda_c$ thickness. The wall is characterized by a dielectric constant of ϵ_r and conductivity σ. The FDTD space is discretised with a resolution of $\lambda_c/10$.

To study the effect of the radar carrier frequency and the wall propagation parameters on the radar signatures, we perform independent simulations at four carrier frequencies - 2.4GHz, 5GHz, 10GHz and 26GHz. The first two frequencies correspond to existing licensed bands for wireless systems that are also being used for indoor radar purposes. The remaining two frequencies are used to provide results that can be compared with other studies on ACR data. The wall parameters - ϵ_r and σ - are varied for each independent simulation. The time-domain simulations are run until they reached steady-state conditions. Then the steady-state time-domain electric field for every point in the FDTD space is Hilbert transformed to obtain the frequency domain response at the desired carrier frequency $E(x, y, f_c)$. We scale the resultant electric field suitably with a constant to obtain the propagation function $H_{ACR}(x, y, f_c)$ for desired transmitted radar power.

The steady-state time-domain electric fields for four carrier frequencies and for two wall conductivity are presented in Fig.3. The top row presents the electric fields for $\sigma = 0.0001S/m$ while the bottom row shows the fields for high $\sigma = 10^5 S/m$. In both cases, we observe the differences in the propagation phenomenology for the different carrier frequencies. When the walls are not very lossy (low σ), the radar signal penetrates through the wall and reaches the corridor space in the NLOS region with respect to the radar. The penetration is greater for the low carrier frequencies when compared to the higher carrier frequencies. We also observe scattering off the lateral surfaces of the wall giving rise to multipath and around the corner of the wall. When the walls are highly lossy, resembling perfect electric conductor conditions, we observe that the through-wall propagation is very low and the signal in the NLOS regions are far higher due to constructive interference from multipath signals scattered off the walls. The results indicate that the dominant electromagnetic propagation mechanism is strongly determined by the carrier frequency and wall conductivity.

A. Electromagnetic radar scattering from a point scatterer in ACR scenarios

We first consider the motion of a point target along a straight-line trajectory. The target starts from a position of $(x_0 = 5.5, y_0 = 2.5)$m and moves along the trajectory shown in the Fig.2 for a duration of 5s at a velocity of $\vec{v} = -1.5\hat{x} + 0\hat{y}$m/s. Therefore, the target is in NLOS conditions with respect to the radar from 0 to 2.73s and from 3.93 to 5s. From 2.73 to 3.93s, the target is within the LOS of the radar. The point scatterer is assumed to have a nonfluctuating radar cross-section of $1m^2$. We simulate the discretised time-domain radar returns, $s_{f_c}[n]$, at carrier frequency f_c using

$$s_{f_c}[n] = H_{ACR}\left(x[n], y[n], f_c\right)^2. \tag{1}$$

where $x[n] = x_0 + v_x n\Delta t$ and $y[n]) = y_0 + v_y n\Delta t$ denote the position along the point target's trajectory at every n^{th} time sample at a sampling frequency of $F_s = \frac{1}{\Delta t} = 1000Hz$. The square in the above expression models the two-way propagation phenomenology, including through-wall physics, multipath scattering, and diffraction. We obtain the time-varying Doppler spectrograms of the target by applying the short-time Fourier transform (STFT) on the radar returns as shown below

$$\chi[n, f] = \sum_{k=1}^{N} x[k]h[k-n]e^{-j2\pi fk/N}. \tag{2}$$

Here N is the number of time samples in the short time window of 0.1s and $h[n]$ is a Hamming window that is applied to mitigate Fourier based side lobes.

Simulation results and analysis: Fig.4 shows the Doppler spectrograms generated for the four carrier frequencies (2.4GHz, 5GHz, 10GHz and 26GHz) for free space and under ACR scenarios with different wall conductivity. The top row of the figure shows the free space results for the four carrier frequencies. The motion of the point scatterer is the same in all the cases and hence the Doppler velocity is the same. However, the time-varying Doppler frequency shown in the figure varies as a function of the carrier frequency

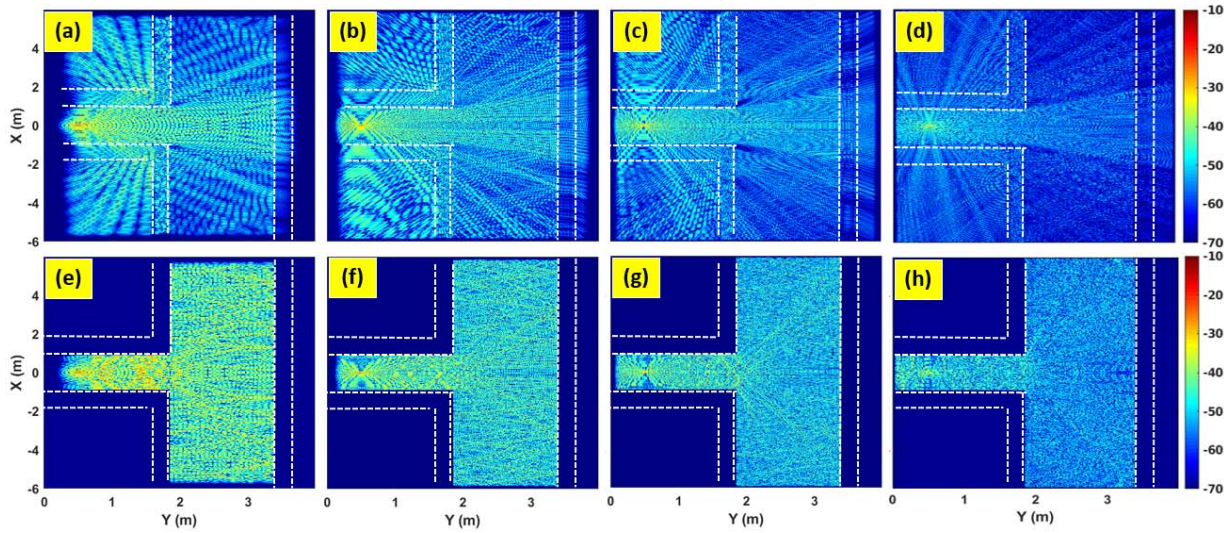

Fig. 3. Top row shows the steady state time-domain electric fields for FDTD space with dielectric walls ($\epsilon_r = 4, \sigma = 0.0001$) at (a)2.4GHz, (b)5GHz, (c) 10GHz and (d)26GHz. The bottom row shows the results for FDTD space with PEC walls ($\epsilon_r = 4, \sigma = 10^5$) at (e)2.4GHz, (f)5GHz, (g)10GHz and (h)26GHz. The walls are indicated with dotted lines.

with the higher carrier frequencies giving rise to higher Doppler frequencies. As the point scatterer walks from 0 to 2.73s in the NLOS region, the Doppler is positive and then it becomes negative in the LOS region when the target tangentially crosses the radar. Then the Doppler becomes negative as the target moves away from the radar. The strongest returns arise at approximately 2.5s when the target is nearest the radar. In all of the four cases, we are able to observe the sidelobes of the Doppler frequency that arise from Fourier processing. Since the sampling frequency is the same across all four cases, we see fewer sidelobes for the higher carrier frequency. The second row shows the returns for the ACR scenarios when the wall conductivity is $\sigma = 0.0001 S/m$. When the wall conductivity is low, the dominant propagation mechanism between the radar and the target is the through-wall propagation especially at lower carrier frequencies. In the NLOS region from 0 to 2.73s, we are able to observe the Doppler returns of the point scatterer for all four carrier frequency. We observe that the strength of the signal is strongest in the case of the 2.4GHz carrier due to penetration of the signal through the walls. For higher carrier frequencies (10GHz and 26GHz), we observe some Doppler spreading from the single point scatterer. These arise from the multipath scattering of the radar signal off the lateral walls. However, since the walls are not very conductive, these returns are weak. The Doppler spreading is most visible from 2.73s to 3.93s when the point scatterer is within the LOS region with respect to the radar. These returns are due to the multiple bounce of the radar returns along the lateral walls of the corridor where the radar is located. The bottom most row shows the Doppler spectrograms when the wall conductivity is very high (equivalent to PEC). Again, we are able to observe the target returns around the corner in the NLOS region. The strength of the signals are even higher than the previous case with the low wall conductivity. This is because the radar signals are not absorbed by the lateral walls and are completely reflected. The regions where the multipath scattering constructively interfere give rise to higher strengths. The Doppler spreads at higher frequencies are now considerable both in the NLOS region and in the LOS region. The results indicate that the multipath Doppler components are enhanced at high carrier frequencies with PEC walls.

B. Electromagnetic radar scattering from dynamic human in ACR scenarios

We extended the formulation in (1) from a single point target to an extended target with multiple point scatterers. If each b^{th} point scatterer has a scattering coefficient a_b and a trajectory $(x_b[n], y_b[n])$, then the time-domain radar returns from the extended target is given by

$$s_{f_c}[n] = \sum_{b=1}^{B} a_b H_{ACR}\left(x_b[n], y_b[n], f_c\right)^2 . \tag{3}$$

The above radar signal model integrates the animation motion of the extended target and the electromagnetic phenomenology of the ACR radar. In this paper, we consider the human as an extended target. The human is a three-dimensional target and is modelled as a combination of 17 primitives - either spheres or ellipsoids - that model the different body parts. The human subject follows the trajectory shown in Fig.5 at a speed of 1m/s for a duration of 5sec. Here, the subject starting from a position $(x_0 = 4.5, y_0 = 2.5)$m, approaches the radar and then turns around and walks away from the radar. The human is assumed to be walking in NLOS conditions with respect to the radar for the entire duration of the motion. The motion of the human and thereby the three-dimensional position of the scattering center of each of the primitives $(x_b[n], y_b[n], z_b[n])$ are obtained from computer animation. The animation data which are described at video frame rates (60 Hz) are interpolated to obtain the motion information at the radar sampling frequency of 1KHz. The three-dimensional human is suitably projected into the two-dimensional FDTD simulation space and appropriate 2D to 3D scaling is carried out to the propagation term $H_{ACR}[x_b, y_b]$ for each position of the scattering center as described in [16]. The strength of the scattering coefficient is obtained from radar cross-section formulae for the primitive shapes for the corresponding carrier frequency. The coefficient is further scaled by the two path loss factor. The strength and positions of the scattering centers are substituted in (3) to obtain the time-domain radar returns.

Simulation results and analysis: We simulate radar returns from a walking human at four carrier frequencies (2.4GHz, 5GHz, 10GHz, and 26GHz) in free space, and then repeat the exercise for different ACR scenarios for two wall conductivity values as discussed the pre-

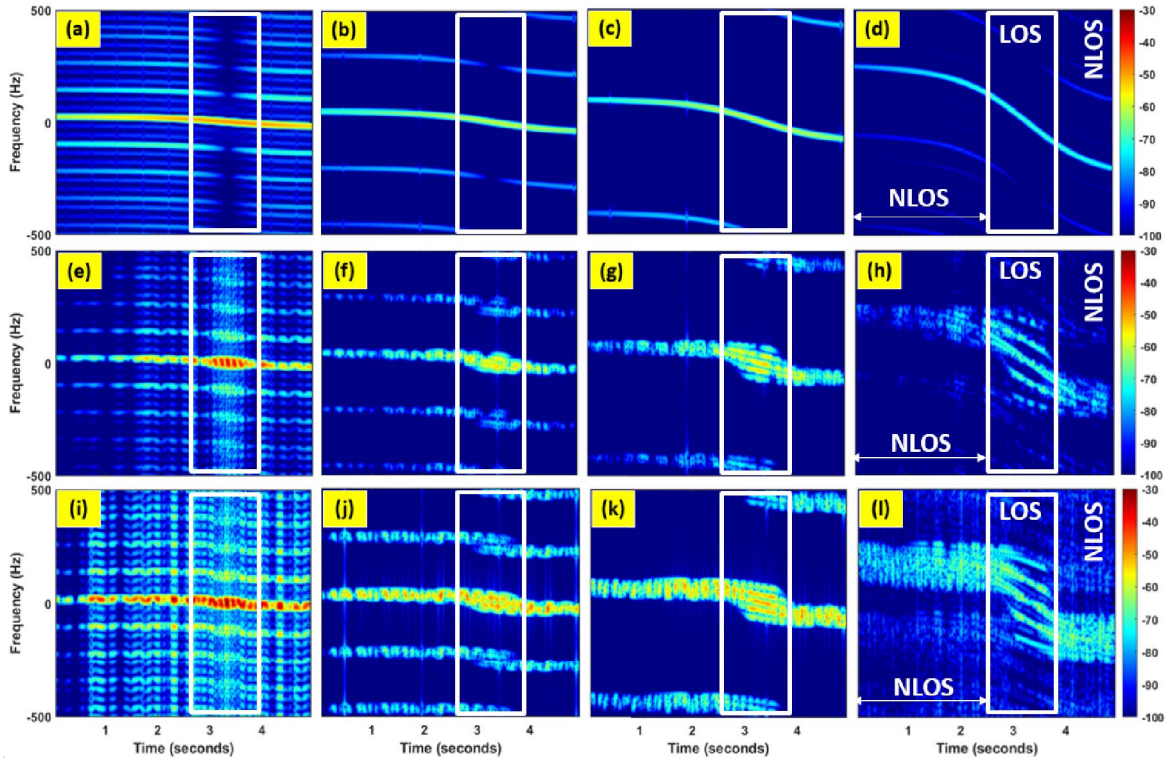

Fig. 4. Spectrograms of a point scatterer in: (a)-(d) free space conditions; (e)-(h) around the corner of a dielectric wall ($\epsilon_r = 4, \sigma = 0.0001$) conditions; and (i)-(l) around the corner of a PEC wall ($\epsilon_r = 4, \sigma = 10^5$) conditions at the carrier frequencies 2.4GHz, 5GHz, 10GHz and 26GHz respectively.

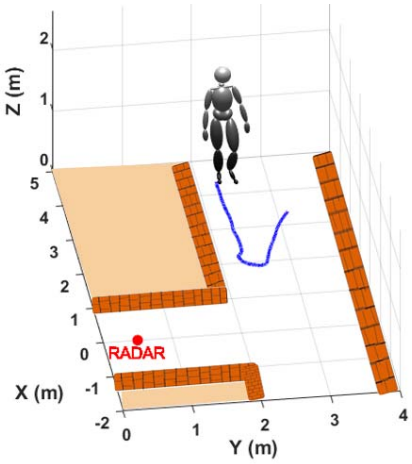

Fig. 5. Trajectory followed by a human in around the corner radar scenario.

vious section. Fig.6 shows the corresponding Doppler spectrograms. The top row shows the micro-Doppler signatures for the different carrier frequencies in freespace conditions. These spectrograms are generated using the short-time Fourier transform with a short time window of 0.1 seconds. Due to the dynamic motion of the arms and legs, each scattering center along the human follows a distinct trajectory, and the resultant Doppler spectrogram show micro-Doppler features. The Dopplers are positive when the human approaches the radar and are negative when the human moves away from the radar. As expected, the Doppler spectrograms corresponding to high carrier frequencies show finer frequency resolution than low carrier frequencies. We kept identical sampling frequency for all the carrier frequencies. Therefore, there is some amount of aliasing at 26GHz.

The second row shows the micro-Doppler returns around the corner when the wall parameters are $\epsilon_r = 4, \sigma = 0.1 S/m$. The parameters are chosen to mimic the realistic ACR scenarios with brick walls. Here, we can observe the micro-Doppler returns for all four carrier frequencies. However, the strength of the returns is highest for the lower frequencies since the through-wall propagation effect dominates at these frequencies. At higher carrier frequencies, we observe micro-Doppler spreading arising due to the multipath scattering off the lateral walls. However, the signal strength is weak since significant energy is absorbed by the walls. The last row shows the spectrograms when the wall conductivity is very high. The strength of the returned signal is highest amongst all the cases, which is possibly due to the constructive interference of the multipath scattering off the lateral walls. The radar signals are completely reflected by the walls. Hence, the Doppler spread is more pronounced at higher frequencies when the wall behaves as PEC.

III. Measurement Experiments

A. Experimental Set Up

We gather measurement data in an ACR scenario using the experimental set up shown in Fig.7. The radar consists of a Field Fox vector network analyzer that can operate from 30KHz to 14GHz. We connect two broad band horn antennas (HF907) at the two ports of the VNA. We configure the VNA to perform narrowband two port scattering parameter measurements. The S_{21} measured by the VNA provides us the time-domain radar returns. The transmitted power of the VNA was set at a maximum of $+3dBm$. The sampling frequency of the VNA is 370Hz. The limited sampling frequency arises due to the hardware limitation of the VNA. We perform independent measurements at three carrier frequencies - 2.4GHz, 5GHz and 10GHz. Based on our current hardware limitations, we could not carry out measurements

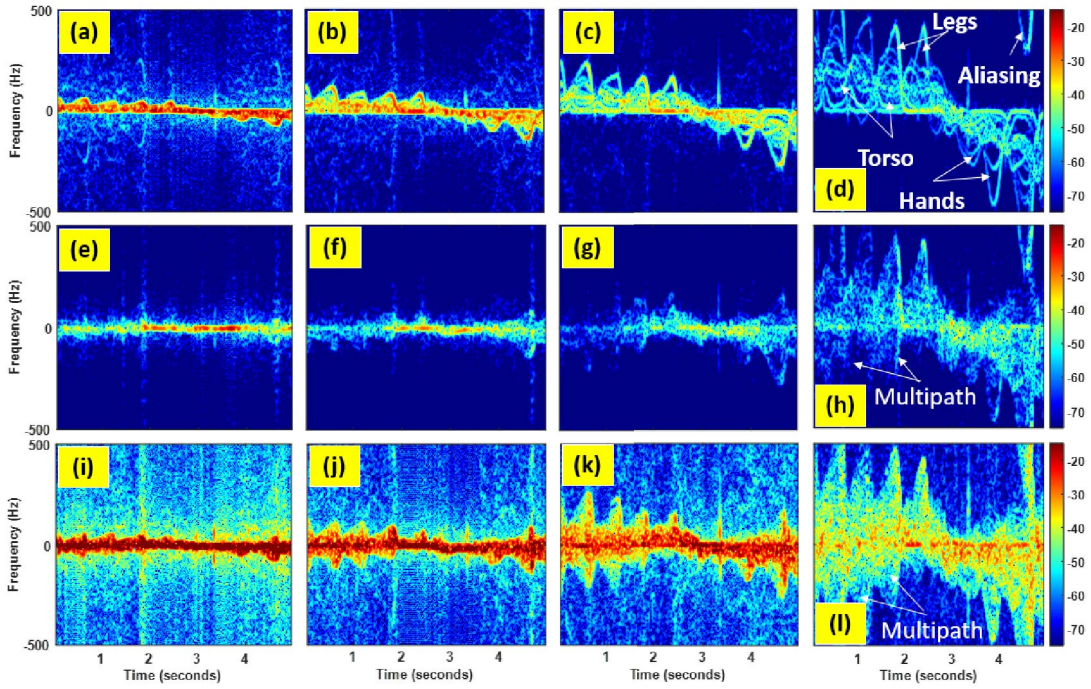

Fig. 6. Spectrograms of a simulated human moving in: (a)-(d) free space conditions, (e)-(h) around the corner of a dielectric wall ($\epsilon_r = 4, \sigma = 0.1$) conditions; and (i)-(l) around the corner of a PEC wall ($\epsilon_r = 4, \sigma = 10^5$) at the carrier frequencies 2.4GHz, 5GHz, 10GHz and 26GHz respectively.

at Ku band. The measurements were first carried out in free space and then repeated in the ACR scenario shown in the figure. The measurement area consists of a T-shaped corridor with 30cm thick brick walls on either side with some doors. The corridor spans 1.8m. The radar is spaced 0.9m behind the edge of the wall as shown in the Fig.7(c). The human walks along a straight line over a distance of 5m at an approximate speed of 1.5m/s and then turns around and moves away. In the ACR scenario, the human is always in the NLOS region with respect to the radar. The horns are tilted so as to ensure that the human is always within the field-of-view of the radar antennas. The human motion was carefully replicated for each measurement. The duration of each measurement is 2.5s.

B. Experimental Results

The micro-Doppler signatures of the human motion in free space and in the ACR scenarios for the three carrier frequencies are shown in Fig.8. The human motion was mostly identical across the free space and ACR conditions. Therefore, the Doppler velocity of the torso and the legs and arms are mostly the same. The top row in the figure shows the micro-Doppler frequencies for the different carrier frequencies. The Dopplers are positive when the human approaches the radar and become zero when the human turns and then become negative as the human moves away from the radar. As expected, the Dopplers are higher for X band when compared to C and S bands. Due to the limited sampling frequency, we do not observe the Fourier sidelobes across the Doppler domain. At X bands, we observe some aliasing of the higher micro-Doppler returns from the human feet at 0.4s.

The bottom row of the figure show the ACR results collected from measurement data for the three carrier frequencies. These returns were obtained from 30cm thick lossy walls. The strength of the returns for all three carrier frequencies is weaker than the free space results. At the lowest carrier frequency, the Doppler returns are observed between 0 and 0.5s when the human is farthest away from the radar. The Doppler returns are at the same band of frequencies as the free space results. This indicates that the dominant propagation mechanism at this frequency is the through-wall propagation. Note the signal travels a two-way propagation path through two walls and hence undergoes significant attenuation. In the case of 5GHz, the ACR returns are only visible from 0.5s on wards. we observe some Doppler spread due to the multipath returns of the radar signals off the lateral walls. However, since real walls are not PEC, the strength of these returns is quite weak. In the case of the X band radar signal, the Doppler spread is significant especially where the human is nearest the radar, when he turns from the radar and begins to walk away. However, the strength of the returns are quite weak. The radar signal does not significantly penetrate the wall. Hence, we do not observe any returns from 0 to 1s.

IV. Conclusion

We have done a detailed experimental study including both simulations and measurements of the effect of wall parameters and carrier frequency on the ACR micro-Doppler signatures. Our study shows that at low carrier frequencies, when the walls are not very lossy, the micro-Doppler signatures show Doppler returns that are similar to those of free space scenarios (except for signal attenuation). This is because the dominant electromagnetic phenomenon is the through-wall propagation. When the walls are more lossy, the multipath resulting from the scattering of the radar signals off the lateral walls form the dominant propagation mechanism giving rise to Doppler spreads. The strength of the signals are often weak due to the absorption of the signals by the walls except in the case of PEC walls where the signals are entirely reflected. Therefore, ACR detection strategies based on multipath scattering require the use of high carrier frequency radars and must account for the nature of the wall characteristics.

References

[1] A. Sume, M. Gustafsson, A. Janis, S. Nilsson, J. Rahm, and A. Orbom, "Radar detection of moving objects around corners," in *Radar Sensor*

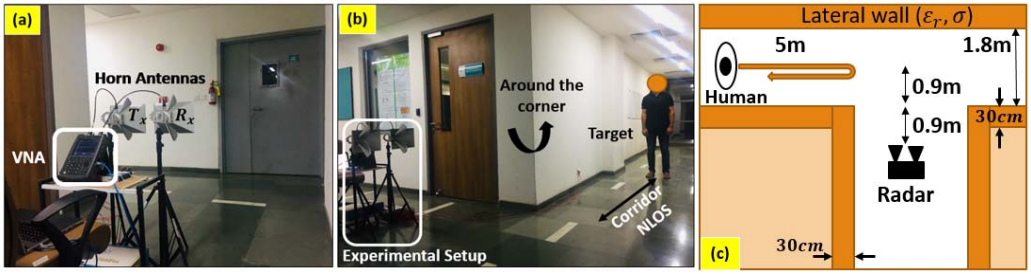

Fig. 7. (a)-(b)Experimental radar setup using N9926A VNA and horn antennas for capturing around the corner reflections and (c) top view image of the room geometry under consideration.

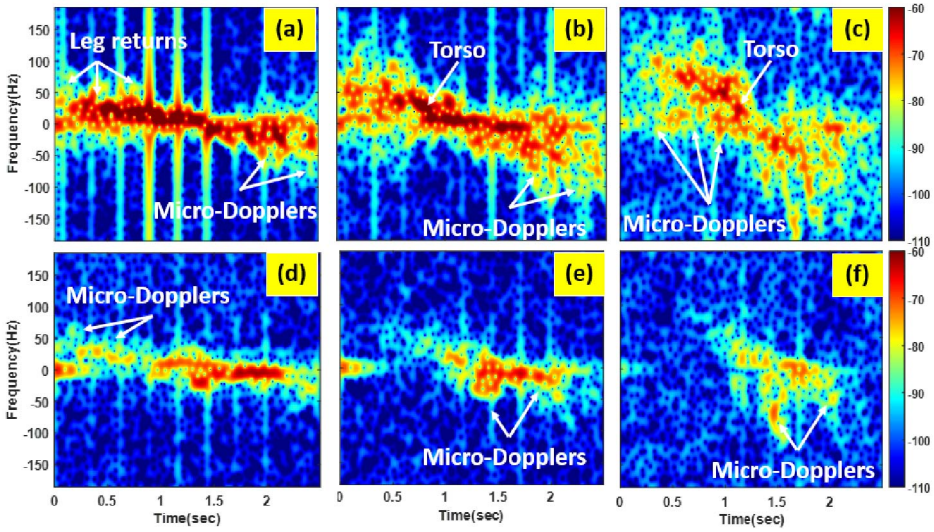

Fig. 8. Spectrogram of a human walking in (a)-(c)LOS conditions and (d)-(f) NLOS condition using around the corner radar at 2.4GHz, 5GHz and 10GHz respectively.

Technology XIII, vol. 7308. International Society for Optics and Photonics, 2009, p. 73080V.

[2] A. Sume, M. Gustafsson, M. Herberthson, A. Janis, S. Nilsson, J. Rahm, and A. Orbom, "Radar detection of moving targets behind corners," *IEEE Transactions on Geoscience and Remote Sensing*, vol. 49, no. 6, pp. 2259–2267, 2011.

[3] O. Rabaste, E. Colin-Koeniguer, D. Poullin, A. Cheraly, J.-F. Petex, and H.-K. Phan, "Around-the-corner radar: detection of a human being in non-line of sight," *IET Radar, Sonar & Navigation*, vol. 9, no. 6, pp. 660–668, 2015.

[4] K.-P.-H. Thai, O. Rabaste, J. Bosse, D. Poullin, I. Hinostroza, T. Letertre, T. Chonavel *et al.*, "Around-the-corner radar: Detection and localization of a target in non-line of sight," in *2017 IEEE Radar Conference (RadarConf)*. IEEE, 2017, pp. 0842–0847.

[5] M. G. Amin, *Through-the-wall radar imaging*. CRC press, 2017.

[6] M. Amin, *Radar for Indoor Monitoring: Detection, Classification, and Assessment*. CRC Press, 2017.

[7] Y. Kim, S. Ha, and J. Kwon, "Human detection using doppler radar based on physical characteristics of targets," *IEEE Geoscience and Remote Sensing Letters*, vol. 12, no. 2, pp. 289–293, 2014.

[8] S. Vishwakarma and S. S. Ram, "Dictionary learning with low computational complexity for classification of human micro-dopplers across multiple carrier frequencies," *IEEE Access*, vol. 6, pp. 29 793–29 805, 2018.

[9] F. Ahmad, M. G. Amin, and G. Mandapati, "Autofocusing of through-the-wall radar imagery under unknown wall characteristics," *IEEE transactions on image processing*, vol. 16, no. 7, pp. 1785–1795, 2007.

[10] F. Ahmad, Y. Zhang, and M. G. Amin, "Three-dimensional wideband beamforming for imaging through a single wall," *IEEE Geoscience and remote sensing letters*, vol. 5, no. 2, pp. 176–179, 2008.

[11] F. Soldovieri and G. Gennarelli, "Exploitation of ubiquitous wi-fi devices as building blocks for improvised motion detection systems," *Sensors*, vol. 16, no. 3, p. 307, 2016.

[12] M. Gustafsson, Å. Andersson, T. Johansson, S. Nilsson, A. Sume, and A. Örbom, "Extraction of human micro-doppler signature in an urban environment using a "sensing-behind-the-corner" radar," *IEEE Geoscience and Remote Sensing Letters*, vol. 13, no. 2, pp. 187–191, 2015.

[13] K.-P.-H. Thai, O. Rabaste, J. Bosse, D. Poullin, I. Hinostroza, T. Letertre, and T. Chonavel, "Detection-localization algorithms in the around-the-corner radar problem," *IEEE Transactions on Aerospace and Electronic Systems*, 2019.

[14] A. Sume and A. Örbom, "See-around-corners with coherent radar. x-band measurements at lilla gåra, august 2007," *Swedish Def. Res. Agency, Linköping, Sweden, Tech. Rep. FOI*.

[15] A. Sume, M. Gustafsson, A. Jänis, S. Nilsson, and A. Örbom, "See-around-corners with coherent radar," in *Proc. 20th Nordic Conf. Radio Sci. Commun., RVK*, 2008, pp. 9–11.

[16] S. S. Ram, C. Christianson, Y. Kim, and H. Ling, "Simulation and analysis of human micro-dopplers in through-wall environments," *IEEE Transactions on Geoscience and remote sensing*, vol. 48, no. 4, pp. 2015–2023, 2010.

[17] S. S. Ram, C. Christianson, and H. Ling, "Simulation of high range-resolution profiles of humans behind walls," in *2009 IEEE Radar Conference*. IEEE, 2009, pp. 1–4.

[18] S. Vishwakarma, V. Ummalaneni, M. S. Iqbal, A. Majumdar, and S. S. Ram, "Mitigation of through-wall interference in radar images using denoising autoencoders," in *2018 IEEE Radar Conference (RadarConf18)*. IEEE, 2018, pp. 1543–1548.